J Solid State Electrochem (2017) 21:873–882
DOI 10.1007/s10008-016-3433-y

ORIGINAL PAPER

High-performance hybrid supercapacitor based on pure and doped $Li_4Ti_5O_{12}$ and graphene

M. Khairy[1,2] · **K. Faisal**[1] · **M.A. Mousa**[1]

Received: 5 July 2016 / Revised: 2 October 2016 / Accepted: 10 October 2016 / Published online: 21 October 2016

Abstract Graphene nanosheets (G) and pure, as well as doped Mg-, Mn-, V-$Li_4Ti_5O_{12}$, spinel structure have been synthesized. As-prepared materials were characterized by X-ray powder diffraction (XRD), FT-IR, scanning electron microscopy (SEM), cyclic voltammetry, and constant current discharge methods. The physical properties, as well as the possible role of the doped materials in supercapacitors, have been studied. The hybrid supercapacitor with pure or doped $Li_4Ti_5O_{12}$ (LTO) anode was fabricated afterward to form the graphene/$Li_4Ti_5O_{12}$. The specific energy, specific power, fast-charge capability, lifecycle, and self-discharge of the studied devices were compared. Metal doping did not change the phase structure while remarkably improved its capacitance at high charge/discharge rate. The hybrid supercapacitor utilizing pure or doped $Li_4Ti_5O_{12}$ as an anode exhibits high capacitance compared to DLC because of the electrochemical process with intercalation/deintercalation of lithium into the spinel LTO. The capacitance of the hybrid supercapacitor decreases from 207 to 108 Fg^{-1} when discharged at several specific current densities ranging from 1 to 10 Ag^{-1}. In contrast, the capacitance of the DLC is slightly decreased.

Keywords Nanoparticles · Hybrid supercapacitor · $Li_4Ti_5O_{12}$ · Graphene · Cyclic voltammetry

✉ M. Khairy
moh_khairy3@yahoo.com

[1] Chemistry Department, Faculty of Science, Benha University, Benha, Egypt

[2] Chemistry Department, College of Science, Al Imam Muhammad Ibn Saud lslamic University, Riyadh, Kingdom of Saudi Arabia

Introduction

As a result of the rapidly growing energy needs of modern life, the development of high-performance energy storage devices has gained significant attention. Supercapacitors are promising energy storage devices with properties intermediate between those of batteries and traditional capacitors [1]. There are two types of supercapacitors depending on energy storage mechanisms, namely, electrical double layer (EDL) capacitors based on ion adsorption and pseudocapacitors based on electrochemical redox reactions [2].

Supercapacitors offer high power density when compared to battery systems and provide a relatively large energy density compared to conventional capacitors. Over the past couple of decades, supercapacitors have become central parts of everyday products by replacing batteries and capacitors in an increasing number of applications. The common supercapacitors now available in the market are symmetric double-layer symmetric capacitors (DLCs) containing activated carbon electrodes and organic electrolytes that deliver cell voltages as high as 3.0 V. Although these DLCs exhibit high power densities and outstanding lifecycle, they suffer from low energy density owing to the limited capacity of C-based electrodes. The specific pseudocapacitance of Faradaic electrodes exceeds that of carbon-based DLCs, but their performance tends to degrade promptly upon cycling. Studies through the past few years have supported an attractive alternative to conventional DLCs and pseudocapacitors by utilizing hybrid systems. Using both Faradaic and non-Faradaic progressions to store charge, hybrid capacitors can attain energy and power densities greater than DLCs without losing the cycling stability and offer ability that has so far limited the success of pseudocapacitors [3].

Such hybrid tactics can overcome the energy density limitation of the conventional electrochemical capacitors

since they employ both the arrangement of a battery-like (faradic) electrode and a capacitor-like (non-faradic) electrode, generating larger capacitance and working voltage [4]. These hybrids can triple the energy density up to 20–30 WhL^{-1} compared to that of conventional electrochemical capacitors. However, the ion exchange rates at the faradic electrodes must be increased to the levels of non-faradic electrodes in order to balance the two systems. To meet these demands, recently, $Li_4Ti_5O_{12}$ (hereafter abbreviated as LTO), which has higher energy density than DLC, has been utilized as an anode material linking with graphene as cathode material in an asymmetric hybrid supercapacitor. The LTO has the following advantages: (1) zero strain insertion that offers little volume change during charge and discharge [5], (2) thermodynamically flat discharge profile at 1.55 V vs. Li/Li^+ [6], (3) high coloumbic efficiency near enough to a theoretical capacity of 175 mAh g^{-1} [7], (4) safety with slight electrolyte decomposition and no gas evolution [8]. In spite of this, the conventional LTO electrode has important drawbacks such as low power characteristics that stem from an inherently low Li^+ diffusion coefficient and poor electronic conductivity [9]. The low conductivity of LTO leads to initial capacity loss and bad rate capability. To enhance the low conductivity, several approaches have been grown, such as cation doping [10], incorporating the second phase with high electronic conductivity, for example, metal powder and carbon [11] and synthesis of the nanosized particle [12].

Various synthesis methods are used for the production of LTO such as hydrothermal [13], sol–gel [14], molten salt [15], solid-state reaction [16], spray pyrolysis [17], and microwave irradiation [18]. Generally, spinel-$Li_4Ti_5O_{12}$ is synthesized by a conventional solid-state reaction using Li_2CO_3 (or LiOH) and TiO_2 as starting materials at high temperatures because the solid-state reaction using Li and Ti source as raw materials is easy and economical [16].

Graphene (G) is an allotrope of carbon as a two-dimensional with one atom thick, a honeycomb cross section in which one atom forms every vertex. Graphene has many amazing properties. It conducts electricity and heat efficiently and has a high mobility of charge carriers [19].

High energy and high power electrochemical energy storage devices depend on diverse essential working principles—bulk vs. surface ion diffusion and electron conduction. Taking on both characteristics has been under deep studies yet, severely hindered by intrinsic material limitations. In this paper, we synthesized G, nanosized pure LTO, and doped (Mg, V, Mn) LTO particles via solid-state reaction and studied the electrochemical properties of both the symmetric and asymmetric hybrid supercapacitor.

Experimental

Materials

All the materials used were of analytical grade.

Preparation of materials

Preparation of graphene nanosheets (G)

Graphene was synthesized by a method similar to the Staudenmaier process with some modifications [20]. First, 5.0 g of graphite (99.99 % purity, provided from Fischer Scientific, Chemical) was slowly added to a mixture of fuming nitric acid (25 ml) and sulfuric acid (50 ml) for 30 min. After cooling the mixture down to 5 °C in an ice bath, 25.0 g of potassium chlorate was slowly added to the solution while stirring for 30 min.

The solution was heated up to 70 °C for 5 h and was then cast on the air for 3 days. Most of the graphite precipitated at the seat, but an exfoliated graphite was floating. The floating carbon materials were moved into DI water (1 L). After stirring it for 1 h, the solution was directly filtrated and the sample was dried in air. The above steps were then repeated four times. Unlike the Staudenmaier process which filters all the graphite powders, we separate out (by filtering) just the floating graphite which has been reacted.

Preparation of pure and doped $Li_4Ti_5O_{12}$

All chemicals were of reagent grades and used as received. Pure and doped $Li_4Ti_5O_{12}$ (LTO) with various dopants (Mg, Mn, and V) were synthesized by using ordinary solid-state reaction. In a typical synthesis, a stoichiometric ratio of starting materials (TiO_2, $LiCO_3$, MgO, MnO_2, V_2O_5) were mixed thoroughly to prepare samples of $Li_{4+x}Ti_5O_{12}$, $Li_{4+x}Mg_{0.1}Ti_5O_{12}$, $Li_{4+x}Mn_{0.1}Ti_{4.9}O_{12}$, and $Li_{4+x}V_{0.1}Ti_{4.9}O_{12}$, where $x = 0, 0.6$. The mixed powders were wetted by absolute ethanol and milled in an energetic ball mill for a week. The obtained slurry was then dried at 80 °C for 1 h, to remove ethanol. Finally, the pure and doped LTO specimens were calcined in an air atmosphere at 800 °C for 4 h.

Characterization

XRD analyses were performed on a Philips X-Ray diffractometer with Cu-$K\alpha$ with $\lambda = 0.154$ nm. The diffractogram was recorded for 2θ angles in the range 15–80°.

The SEM photographs were taken with a scanning electron microscope (Philips SEM 515).

The FT-IR spectra were recorded in the range of 400–4000 cm^{-1} using an infrared spectrophotometer (Perkin-Elmer LX 18–5255).

The surface properties, namely, the BET surface area, pore volume (*Vp*), and mean pore diameter (*r*), were determined from N_2 adsorption–desorption isotherms measured at 77 K using conventional volumetric apparatus. The samples were evacuated at 473 K for 3 h under a reduced pressure of 10^{-5} Torr before starting the measurement.

Electrochemical measurements

The pure and doped LTO anodes were prepared by mixing the active material with conductive carbon black (Super P) and polyvinylidene fluoride (PVDF) as a binder with the weight ratios 80:10:10, respectively. N-methyl pyrrolidiznone (NMP) was utilized as a solvent. The slurry obtained from the mixture was coated on a copper current collector and dried at 150 °C to remove the NMP solvent. In the case of graphene electrode, the conductive material was not included in the electrode preparation. Few drops of n-methyl pyrrolidinone (NMP) were added to form slurry. The charge and discharge measurements were carried out in a cylindrical cell (2245 size). The asymmetric hybrid supercapacitor cells were assembled by using pure and doped LTO as an anode and graphene as a cathode. To compare the asymmetric hybrid supercapacitor, G-double-layer symmetric capacitor (DLC) cell was fabricated in the same way. The mass ratio of positive to negative electrodes was evaluated by using the following equation to maintain a charge balance: $q+ = q-$ in order to fabricate the device $m^{+}/m^{-} = (C_{-} \times \Delta E_{-}) / (C_{+} \times \Delta E_{+})$ in which $q+/q-$, $m+/m-$, $C+/C-$, and $E+/E-$ are the charge, mass, specific capacitance, and potential windows for the cathode (+)/anode (−), respectively. Accordingly, the optimal positive-to-negative mass ratio was determined to be 1: 2.5 of LTO/G for the asymmetric capacitor.

The electrolyte was a 1 M solution of $LiPF_6$ in ethylene carbonate (EC)-dimethyl carbonate (DMC) 2:1 in *v/v*. Non-woven fabric was utilized as the separator. All electrochemical characterization was performed in the two-electrode system at room temperature. *EIS* and CV were conducted using an Autolab (Metrohm analyzer). Galvanostatic charge–discharge measurements were performed using LAND CT2001A model test system.

Results and discussion

XRD patterns of graphene (G) (Fig. 1) dominate reflection peak centered at $2\theta = 24°$ (002), which is correlated to an interlayer spacing of 0.38 nm. The observed broad peak also indicates that the graphene sheets are loosely stacked in G, and it is different than that of the crystalline graphite. The absence

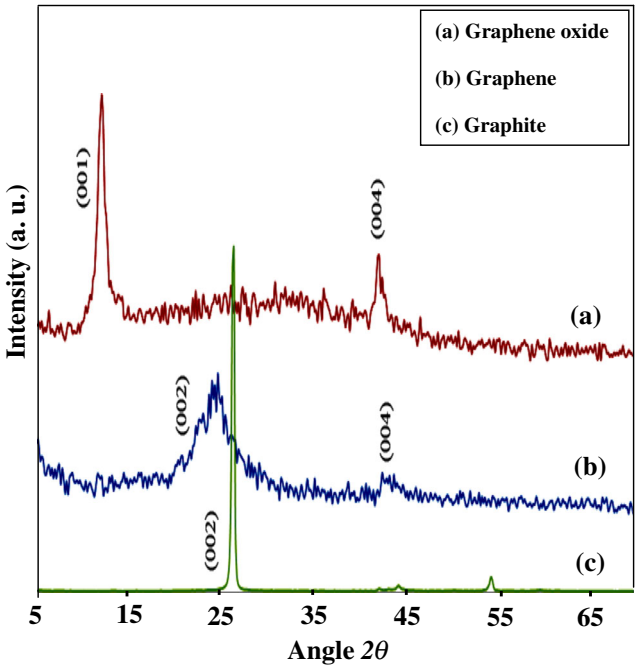

Fig. 1 XRD patterns of **a** graphene oxide, **b** reduced graphene, and **c** graphite

of any peak characterized for graphene oxide or graphite indicates that the prepared sample is pure graphene. The crystallite size of G is estimated by Debye Formula [21]: $D = 0.9\lambda/\beta\cos\theta$, where *D* is the average crystallite size, λ is the wavelength of Cu-$K\alpha$, β is the full width at half maximum (*FWHM*) of the diffraction peaks, and θ is the Bragg's angle, and the average size of particles is calculated to be about 3 nm (Table 1).

XRD patterns of either pure or doped LTO specimen with a stoichiometric ratio of 4:5 and 4.6:5 was shown in Fig. 2. The XRD patterns of pure LTO specimen with a stoichiometric ratio of 4:5 (Fig. 2e) illustrated the formation of LTO cubic spinel phase structure as the main product with diffraction peaks at 18°, 37°, 43°,49°, 58°, 63°, 66°, 75°, 76°, and 79° referring to (111), (311), (400), (331), (333), (440), (531), (532), (622), (444), (JCPDS card no. 49–0207), respectively. Besides these major peaks, some impurity phases matching to

Table 1 Lattice parameter *a*, particle size, and surface properties of spinel $Li_4Ti_5O_{12}$ and $Li_4Ti_5O_{12}$ doped with Mg, Mn, and V as well as graphene

Sample	Crystallite size (nm)	Lattice parameter (*a*) (Å)	Surface area ($m^2\ g^{-1}$)	Pore diameter (nm)	Pore volume (ml)
LTO	156	8.350	33	28.15	0.037
Mg-LTO	102	8.352	46	20.13	0.037
Mn-LTO	127	8.338	38	25.60	0.039
V-LTO	135	8.343	34	20.19	0.027
G	3	–	179	34.80	0.249

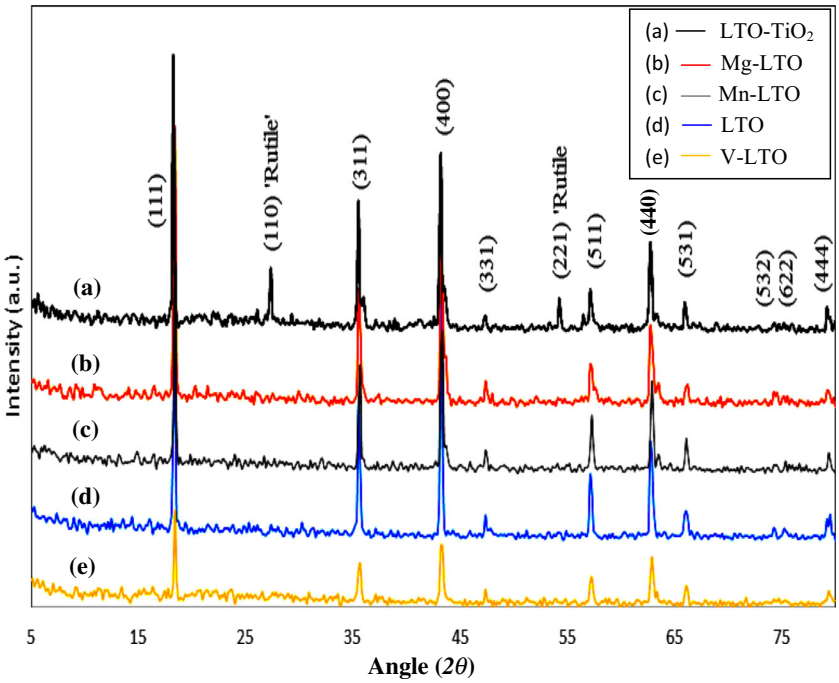

Fig. 2 XRD patterns of **a** LTO-TiO_2, **b** Mg-LTO, **c** Mn-LTO, **d** LTO, and **e** V-LTO

a rutile TiO_2 phase at 27° and 55° (JCPDS card no. 76–1940) were also observed. This means that not all amounts of TiO_2 reacted with Li_2CO_3. Subsequently, we have prepared other pure and doped samples under the same conditions used previously but with a stoichiometric ratio of Li/Ti equal to 4.6:5 (i.e., in presence excess of Li). XRD of these specimens (Fig. 2a) illustrated the formation of pure cubic spinel phase structure of $Li_4Ti_5O_{12}$ with a Fd3m space group in addition to a small end hump at 43.7° and 63.5° ascribed to the (400) and (440) crystal faces of Li_2TiO_3 (JCPDS no. 74-2257). These results coincide with the data obtained from a phase diagram of TiO_2–Li_2CO_3 [22].

The results obtained point to that the dopants have successfully inserted into the spinel lattice structure of $Li_4Ti_5O_{12}$ without causing any changes in its structural characteristics. The crystallite sizes of the studied samples were calculated by the Debye formula, and the values obtained are listed in Table 1, from which it can be seen that the crystallite size decreases through introducing doping ions into LTO lattice. It decreases in the order Mg-LTO < Mn-LTO < VLTO < LTO.

Bragg's equation was applied to determine the lattice parameter, a, by $n\lambda = 2d_{hkl}\sin\theta$, where n is 1, λ is the wavelength of the incident X-ray beam (0.154 nm), θ is the incident angle, and d is the distance between the atomic layers of the cubic structure. Because $Li_4Ti_5O_{12}$ is a face-centered cubic, the lattice parameter is evaluated by using $d_{hkl} = a/L$, with $L = (h^2 + k^2 + l^2)^{0.5}$, where (hkl) are the Miller indices. The lattice parameters evaluated for the pure and doped samples are listed in Table 1. The "a" values obtained is in harmony with the modification of the ionic radii induced by the individual substitution. Since ionic radii of Mg^{2+}, Mn^{4+}, and V^{5+} are 0.066, 0.06067, and 0.05968 nm, which are smaller than Ti^{4+} and Li^+ (0.068 nm), the lattice parameters a of all substitutions, except for Mg-LTO, were smaller than the spinel $Li_4Ti_5O_{12}$.

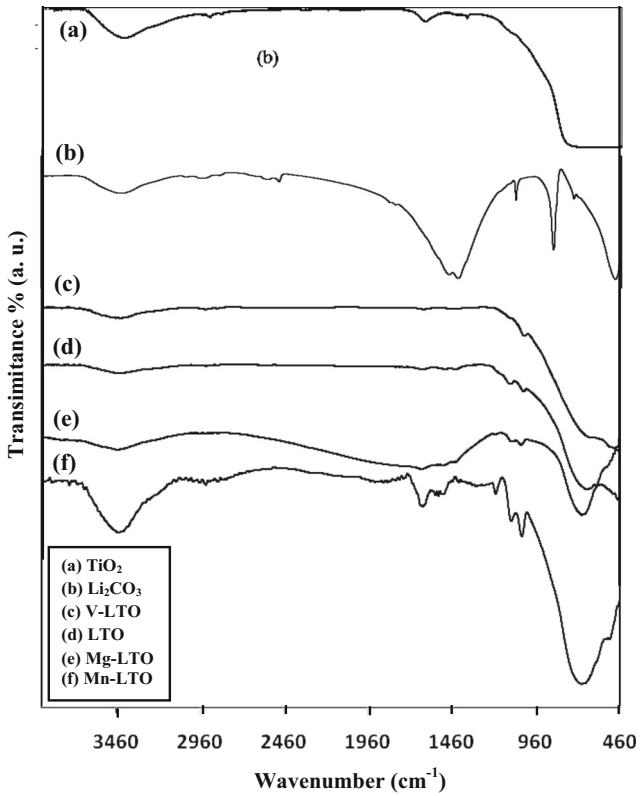

Fig. 3 FT-IR spectra of **a** TiO_2, **b** Li_2CO_3, **c** V-LTO, **d** LTO, **e** Mg-LTO, and **f** Mn-LTO

The increase in the lattice constant parameter of Mg-LTO specimen might be due to the fact that the substitution of doping ions for Ti^{4+} site will produce the transition of a certain amount of Ti^{4+} to Ti^{3+} as charge compensation [23], which will cause the increase of the lattice constant of the $Li_4Ti_5O_{12}$ because Ti^{3+} (0.069 nm) is larger than Ti^{4+} (0.068 nm).

Figure 3a–f shows FT-IR of Li_2CO_3, TiO_2, pure and doped LTO. It demonstrates a vibration band at ~3400 cm^{-1} for adsorbed H_2O molecules, 1482 cm^{-1} and 1426 cm^{-1} for carbonate group, 1088 cm^{-1} for Li-O band, and 583 cm^{-1} for Ti-O band. The FT-IR spectra of calcined mixtures, with Li/Ti ratio of 4.6:5 at 800 °C illustrated the absence of vibration bands of the carbonate group, which shows that all Li_2CO_3 reacted (Fig. 3c–f). The figure demonstrates a band at 1621 cm^{-1} corresponding to the vibration of adsorbed H_2O molecules, whereas the band of Li-O and Ti-O still appeared in the range from 450 to 1000 cm^{-1}.

The surface morphology and particle sizes of pure, doped LTO and graphene samples were examined using SEM and given in Fig. 4a–e. The images of pure and doped LTO show that these samples are well crystallized. Moreover, it is clear that doping does not change the morphological aspect of the doped LTO nanoparticles when compared with pure LTO and hence the same cubic morphology is maintained in the case of doped LTO also. On the other hand, the image of graphene (Fig. 4e) shows graphene sheets stacked together with the presence of pore inside the sheet. The diameter of the plate-like stacked morphology lie in the range 1–2 μm.

Information on the surface characteristics of a material is essential for the possible applications of surfaces in

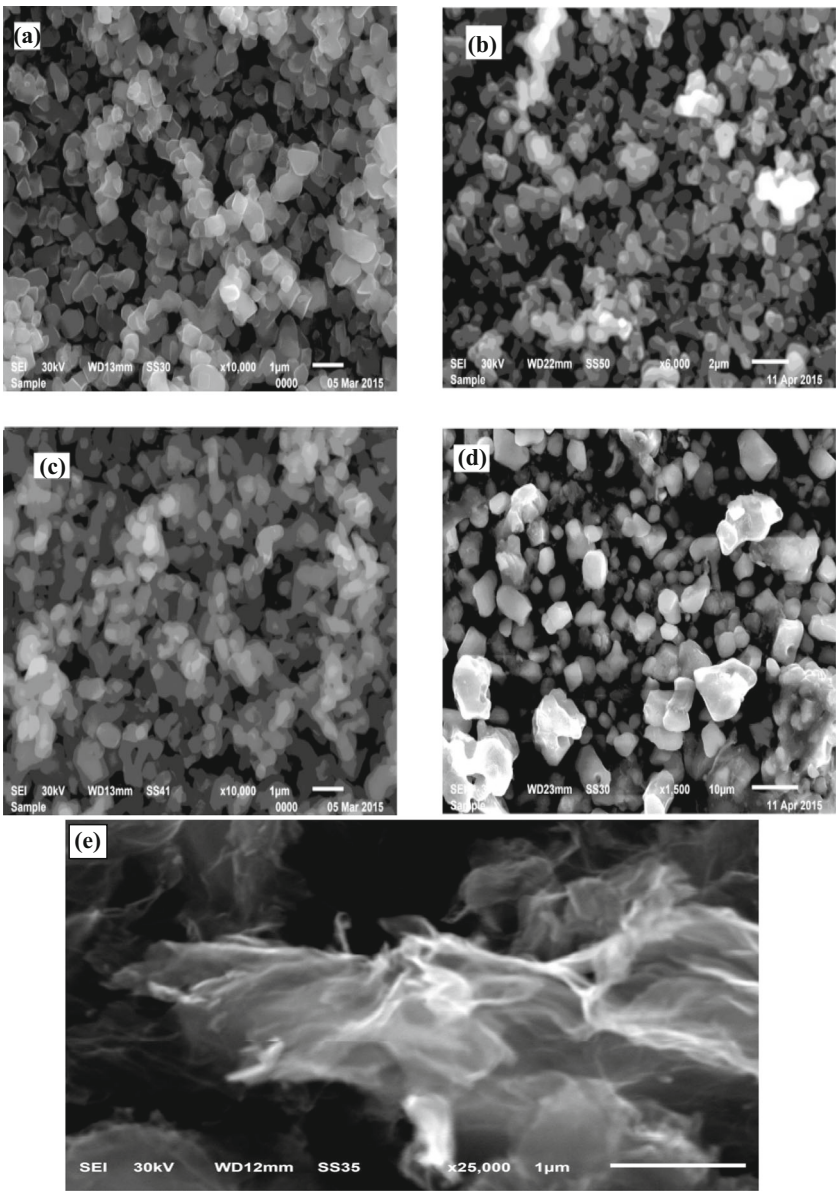

Fig. 4 SEM images of **a** LTO, **b** Mg-LTO, **c** Mn-LTO, **d** V- LTO and **e** G.

electrochemical research [24]. The surface textures of the samples investigated were examined from the N_2 adsorption/desorption isotherms (Fig. 5). The isotherm of all samples exhibits type IV characteristics according to the IUPAC classification, indicating the presence of mesoporous morphology. The hysteresis loops of type H3 are observed and characteristic to aggregates of plate-like or slit-shaped pores [25]. The Brunauer–Emmett–Teller (*BET*) method has been used to determine the surface area for the electrode materials in the range of $0.05 < p/p° < 0.35$. The pore size distribution of the samples is calculated using the Barrett–Joyner–Halend (*BJH*) method. The surface data of the specimens investigated are listed in Table 1, from which it can be seen that the surface area increases in the order: G > Mg-LTO > Mn-LTO > V-LTO > pure LTO. This reveals that the surface area of LTO specimens increases with introducing doping ions into the LTO lattice. On the other hand, the pore diameters of the doped LTO samples are less than that of the pure one according to the consequence: V-LTO < Mg-LTO < Mn-LTO < pure LTO. Generally, the mesoporous structure obtained for the electrode materials

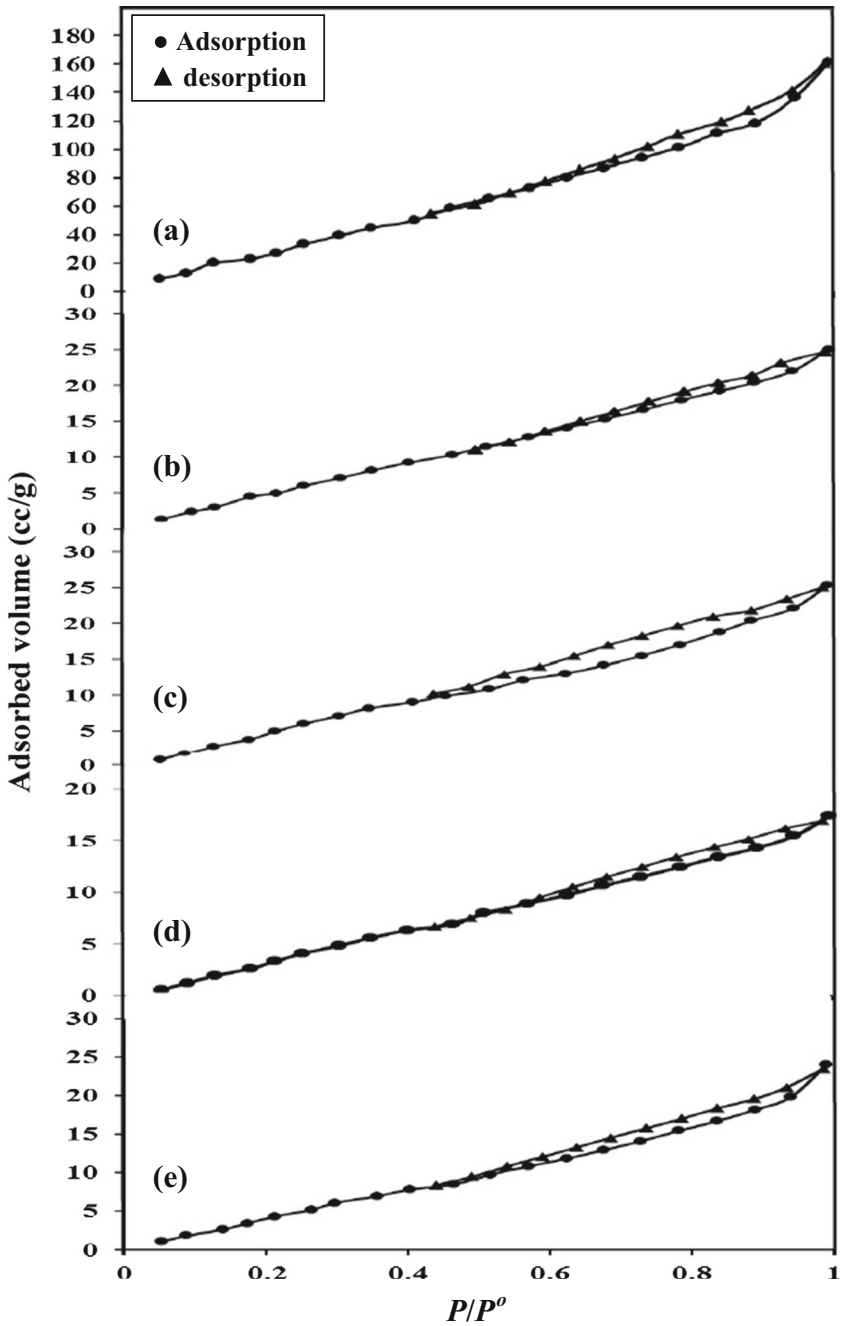

Fig. 5 N_2 adsorption-desorption isotherms of **a** G, **b** Mn-LTO, **c** Mg-LTO, **d** V-LTO, and **e** LTO

can play a major role to the high-performance of the supercapacitor devices due to the fast diffusion of ions improving electrolyte access to the high interfacial area.

Cyclic voltammetry (CV) is known as a tool suitable to indicate the difference between non-faradaic reaction and faradaic reaction. Figure 6 shows the results of cyclic voltammetry for the studied cells at 5 mV/s.

The CV curve of G/G (DLC) exhibits a semirectangular shape with no obvious peaks, which is a characteristic of the electric double-layer capacitance of carbon-based materials. On the other hand, pure or doped LTO/graphene (asymmetric capacitors) clearly show a different electrochemical behavior (Fig. 6b), where the cathode (G) stores charge through an electrostatic adsorbing–desorbing process on the surface of G. On the other hand, the anode (pure or doped LTO) exhibits an oxidation–reduction behavior (can be better seen at a higher scanning rate) [26].

The specific capacitance (C) was calculated from CV data according to Eq. (1) [27].

$$C = \frac{2}{\Delta V.\upsilon.m}\int_{-V}^{+V} I(V)dV \quad (1)$$

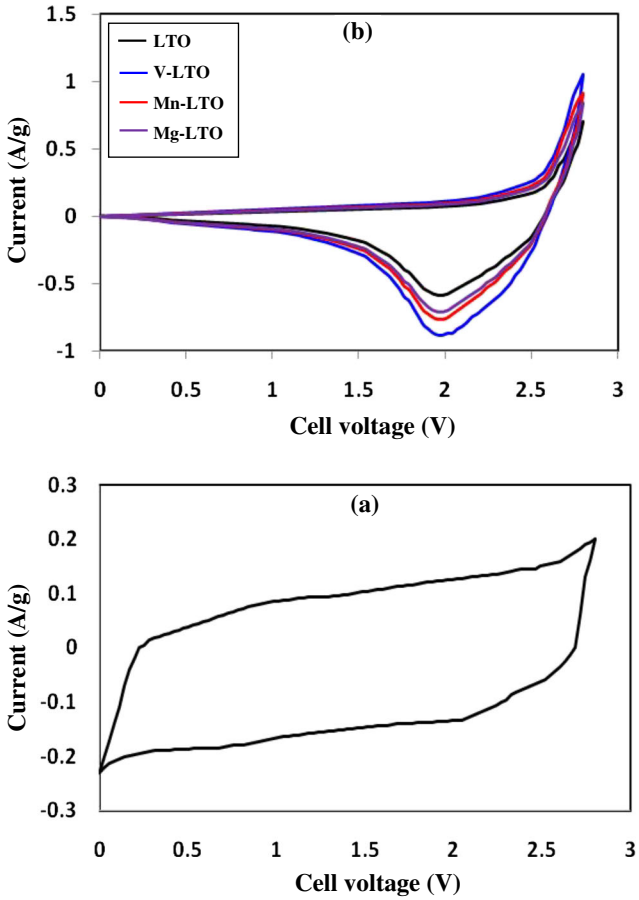

Fig. 6 Cyclic voltammetric curves (CVs) of DLC G/G (**a**) and the hybrid-supercapacitor G/$Li_4Ti_5O_{12}$ (pure and doped) (**b**)

where C is specific capacitance, V is potential, ( ) (ν) is scan rate, I is current, and m is a mass of active material of the electrode. The results obtained are summarized in Table 2. It shows that the capacitance increases according to the order

G/V−LTO > G/Mn−LTO > G/Mg−LTO > G/LTO > G/G

Figure 7 shows the discharge curves of the DLC and hybrid capacitors (cutoff voltage 2 V) at discharge current 1 A. Capacitances were calculated from each discharge curve and the results obtained are given in Table 2. The capacitance values of the hybrid supercapacitors are about two times of DLC and higher for doped LTO cells compared with pure one. The differences of the discharge time and specific capacity between the hybrid supercapacitors and DLC reveal that the hybrid supercapacitor cell is composed of the capacitor system and the secondary battery system, as described according to the following equations:

$$G + PF_6^- \rightleftharpoons G^+ \bullet PF_6^- + e^- [\text{cathode}]$$

$$Li_4Ti_5O_{12} + 3Li^+ + 3e^- \rightleftharpoons Li_7Ti_5O_{12} [\text{anode}]$$

The graphene electrode shows a double-layer electric behavior due to the electrostatic adsorbing–desorbing process of PF_6^- on G. On the other hand, the LTO electrodes exhibit an oxidation–reduction behavior.

The energy density (E, Wh kg^{-1}) and power density (P, W kg^{-1}) were derived from CV curves at various scan rates using Eqs. (2) and (3), respectively [28]:

$$E = \frac{1}{2}C_s(\Delta V)^2 \quad (2)$$

$$P = \frac{E}{t} \quad (3)$$

where C_s is the specific capacitance calculated from the charge/discharge curve in Fg^{-1}, ΔV is the voltage change during the discharge process, and t is the discharge time in h. Results (Table 2) show that the energy density of the hybrid supercapacitor is higher than DLC, whereas its power density is worse.

Table 2 Electrochemical results: capacitance obtained from CV at 5 mv/s and discharge current at 1 A

Capacitor	Capacity (Fg^{-1})	E (Wh kg^{-1})	P (W kg^{-1})
G/G	42 (50)	11.7	461
G/LTO	162 (140)	45.5	759
G/Mg-LTO	170 (184)	47.8	771
G/Mn-LTO	186 (202)	52.3	850
G/V-LTO	207 (223)	58.2	831

( ) Values from CV data

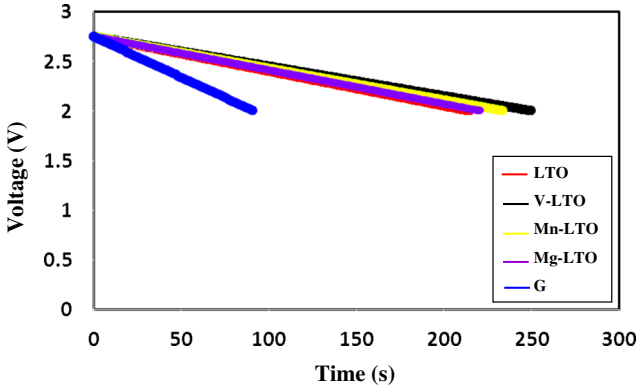

Fig. 7 Discharge curves of DLC and hybrid capacitors (discharge current 1 A)

Figure 8 shows cycle performances of the hybrid supercapacitor and DLC. After 5000 cycles, capacitance losses of the DLC, LTO/G, Mg-LTO/G, Mn-LTO/G, and V-LTO/G are 7.0, 10.8, 11.3, 11.1, and 11.5 %, respectively. Results reveal that the cycle performance of hybrid supercapacitors is slightly worse than that of DLC. However, the capacitance values of the hybrid supercapacitors are higher than the double value of DLC. This result indicates that the energy storage performance of hybrid supercapacitors is better than that of DLC.

For rate capability, both DLC (G/G) and the hybrid capacitor V-LTO/G were tested at various discharge rates. Their charge/discharge current densities were the same for comparison purposes. From the results obtained, shown in Fig. 9, it can be seen that the capacitance decreases slightly with increasing discharge rate for DLC and that it decreases obviously for the hybrid capacitors due to the polarization effect. These outcomes demonstrate DLC has good performance at high charge/discharge rates compared with the hybrid capacitor because of its electrostatic storage mechanism.

Impedance spectroscopy (EIS) is an ideal tool for characterizing electrochemical capacitor because it provides

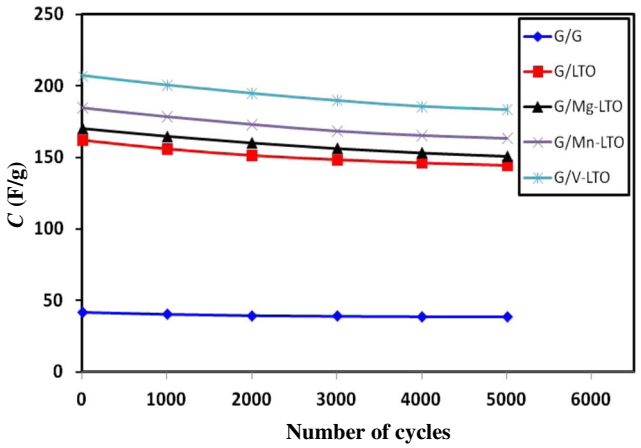

Fig. 8 Cycle stability of DLC and hybrid capacitors during the long-term charge/discharge process at a current density of 1 Ag^{-1} and voltage range from 0 to 2.8 V

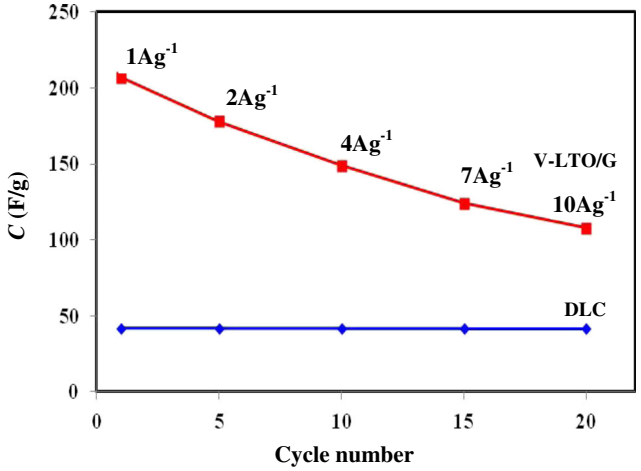

Fig. 9 Discharge curves of DLC and hybrid capacitors at different discharge current densities

important information on the timescales of all phenomena occurring in the capacitor and knowing the parameters involved in each step of the electrochemical process. In general, EIS is exhibited as a Nyquist plot by employing a real number measure (Z_{re}) of the impedance as the X axis and an imaginary number quantity (Z_{im}) of the impedance as the Y axis. Figure 10 shows Nyquist plots for the four capacitor cell configurations studied. All the impedance spectra are similar in shape to an arc in the higher frequency region and a spike in the low-frequency region, demonstrating a capacitive behavior. The semicircle at the high frequency range is associated with the charge transfer resistance at the active material interface, while the inclined line at the low frequency ending attributes for the Warburg factor being related to the diffusion-controlled process of the Li ions. From the high frequency intercept of the semicircle with the real axis, the equivalent series resistance (ESR) may be determined. For symmetric cell (G/G), the nearly vertical line at the low-frequency region

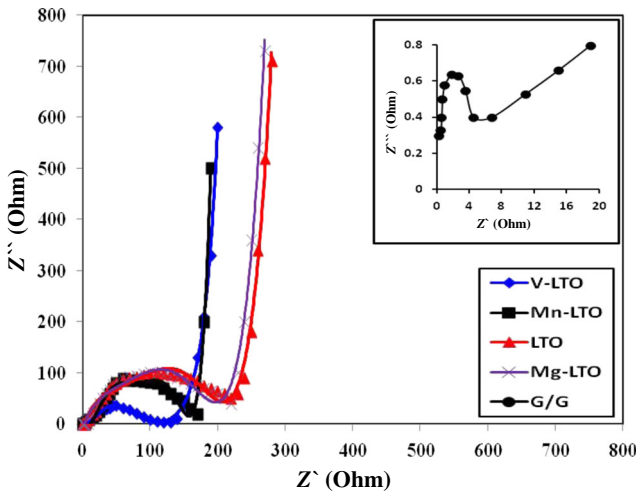

Fig. 10 Impedance plots at room temperature for LTO, Mg-LTO, V-LTO, and Mn-LTO. The inset is the impedance plots of (*black circle*) G/G

is a good hint of a pure capacitive behavior with a low diffusion resistance of ions in the structure of the electrode due to the mesoporous surface network, which provides better accessibility to the ions in the electrolyte. For asymmetric cells, the impedance spectra are similar in shape with the exception of the small change of equivalent series resistance (ESR) in the high-frequency range; this represents a combined resistance from the ionic resistance of the electrolyte and the intrinsic/contact resistance produced by the interfaces. As shown in Fig. 9, there is a significant difference among dopants. And, the value of the diameter for the semicircle on the Z` axis approximately amounts to be 5, 230, 220, 160, and 100 Ω, for G/G, LTO/G, Mg-LTO/G, Mn-LTO/G, and V-LTO/G, respectively. This refers to that the values of R_{ct} for the LTO electrodes following the order: LTO > Mg-LTO > Mn-LTO > V-LTO. This refers to that the doped ions improved the electronic conductivity of doped LTO compared to a pure one. Figure 10 also shows that the charge transfer resistance of V-LTO is much lower than that of any other specimen investigated. The hopping transport of the 3D electrons via the V^{5+} or Mn^{4+} and Ti^{4+} ions is feasible because the Mn and V 3D bands are close to the Ti 3D ones [29]. In the case of Mg-LTO, the valence of titanium is influenced by the valence of magnesium. Thus, the substitution of Li^+ by Mg^{2+} led to mixed Ti^{4+}/Ti^{3+} valences and enhanced the conductivity of LTO.

Conclusions

In conclusion, nanoparticles LTO and Mg-, V-, or Mn-LTO were successfully synthesized using a solid-state reaction method. The effect of doping on the crystal structure and morphology was investigated. It could be concluded that Mg^{2+}, Mn^{4+}, and V^{5+} ions do not change the cubic spinel nature of the LTO and also no morphological changes. The effect of doping content on the electrochemical performance of the as-synthesized samples was preliminarily investigated. It is apparent from the electrochemical studies carried out that doping greatly influences the cyclic behavior and thereby improves the functioning of the electrode material. The results revealed that the V-LTO sample exhibited the largest specific capacity and the best rate capability among all the prepared electrodes. It is a valuable material as an anode for lithium-ion batteries applied in large-scale energy storage.

References

1. Harrop DP, Zhitomirsky, DV (2013) Electrochemical DLC supercapacitors 2013–2023, business report IDTechEx, July 2013. Available at www.idtechex.com. Accessed March, 2015
2. Wang G, Zhang L, Zhang J (2012) A review of electrode materials for electrochemical supercapacitors. J Chem Soc Rev 41:797–828
3. Long JW, Bélanger D, Brousse T, Sugimoto W, Sassin MB, Crosnier O (2011) Asymmetric electrochemical capacitors-stretching the limits of aqueous electrolytes. J MRS Bull 36:513–522
4. Simon P, Gogotsi Y, Dunn B (2014) Materials science. Where do batteries end and supercapacitors begin?. Science 343:1210–1211
5. Jo MR, Lee GH, Kang YM (2015) Controlling solid- electrolyte-Interphase layer by coating P-type semiconductor NiOx on $Li_4Ti_5O_{12}$ for high-energy-density lithium-ion batteries. J ACS Appl Mater Interfaces 7:27934–27939
6. Thackeray MM (1995) Structural considerations of layered and spinel lithiated oxides for lithium ion batteries. J Electrochem Soc 142:2558–2563
7. Jansen AN, Kahaian AJ, Kepler KD, Nelson PA, Amine K, Dees DW, Vissers DR (1999) Development of a high-power lithium-ion battery. J Power Sources 81-82:902–905
8. Goripart S, Miele E, Angelis FD, Fabrizio ED, Zaccaria RP, Capiglia C (2014) Review on recent progress of nanostructured anode materials for Li-ion batteries. J Power Sources 257:421–443
9. Baohua L, Feng N, Yan-Bing H, Hongda D, Quan-Hong Y, Jun M, Feiyu K, Chin-Tsau H (2011) Synthesis and characterization of long life $Li_4Ti_5O_{12}$/C composite using amorphous TiO_2 nanoparticles. Int J Electrochem Sci 6:3210–3223
10. Yi TF, Shu J, Zhu YR, Zhu XD, Zhu RS, Zhou AN (2010) Advanced electrochemical performance of $Li_4Ti_{4.95}V_{0.05}O_{12}$ as a reversible anode material down to 0V. J Power Sources 195:285–288
11. Huang S, Woodson M, Smalley R, Liu J (2004) Growth mechanism of oriented long single walled carbon nanotubes using "fast-heating" chemical vapor deposition process. J Nano Lett 4:1025–1028
12. Jung HG, Jang MW, Hassoun J, Sun YK, Scrosati B (2011) A high-rate long-life $Li_4Ti_5O_{12}$/$Li[Ni_{0.45}Co_{0.1}Mn_{1.45}]O_4$ lithium-ion battery. J Nature Communications 2:516. doi:10.1038//ncomms1527
13. Li J, Tang J, Zhang Z (2005) Controllable formation and electrochemical properties of one-dimensional nanostructured spinel $Li_4Ti_5O_{12}$. J Electrochem Commun 7:894–899
14. Kavana L, Grätzel M (2002) Facile synthesis of nanocrystalline $Li_4Ti_5O_{12}$ (spinel) exhibiting fast Li insertion. J Electrochem Solid-State Lett 5:A39–A41
15. Yuan T, Cai R, Wang K, Ran R, Liu S, Shao Z (2009) Combustion synthesis of high-performance $Li_4Ti_5O_{12}$ for secondary Li-ion battery. J Ceram Inter 35:1757–1768
16. Yao W, Zhuang W, Wang XJ (2016) Solid state synthesis of $Li_4Ti_5O_{12}$ hiskers from TiO_2-B. J Mater Res Bull 75:204–210
17. Birrozzi A, Copley M, Zamory J, Pasqualini M, Calcaterra S, Nobili F, Cicco AD, Rajantie H, Briceno M, Bilbé E, Cabo-Fernandez L, Hardwick LJ, Bresser D, Passerini S (2015) Scaling up nano $Li_4Ti_5O_{12}$ for high-power lithium- ion anodes using large scale flame spray pyrolysis. J Electrochem Soc 162:A2331–A2338
18. Nowack LV, Waser O, Yarema O, Wood V (2013) Rapid, Microwave-assisted synthesis of battery-grade lithium titanate (LTO). J RSC Adv 3:15618–15621
19. Rao CNR, Sood AK (2013) Graphene: synthesis, properties, and phenomena. Wiley-VCH Verlag GmbH & Co. KgaA. doi:10.1002/9783527651122.ch1
20. Sheshmani S, Fashapoyeh MA (2013) Suitable chemical methods for preparation of graphene oxide, graphene and surface functionalized graphene nanosheets. J Acta Chim Slov 60:813–825
21. Klug HP, Alexander LE (1970) X-ray diffraction procedures. Wiley, New York
22. Laumann A (2010) Novel Routes to $Li_4Ti_5O_{12}$ spinel: chatacterization and phase relations, Thesis, Facultät für Geowissenshaften der Ludwig Maximilians, Munchen University, Germany, 1

23. Sun X, Radovanovicb PV, Cuia B (2015) Advances in spinel $Li_4Ti_5O_{12}$ anode materials for lithium-ion batteries. J New J Chem 39:38–63
24. Mingjia Z, Chengcheng X, Jiangtian L, Ming L, Nianqiang W (2013) Nanostructured carbon–metal oxide composite electrodes for supercapacitors: a review. Nanoscale 5:72
25. Gregg SJ, Sing KSW (1967) The adsorption, surface area and porosity. Academic, London
26. Woo SW, Dokko K, Kanamura K (2007) Preparation and characterization of three dimensionally ordered macroporous $Li_4Ti_5O_{12}$ anode for lithium batteries. Electrochim Acta 53:79–82
27. Han D, Xu P, Jing X, Wang J, Yang P, Shen Q, Liu J, Song D, Gao Z, Zhang M (2013) Trisodium citrate assisted synthesis of hierarchical NiO nanospheres with improved supercapacitor performance. J Power Sources 235:45–53
28. Simon P, Gogotsi Y (2008) Materials for electrochemical capacitors. J Nature Mater 7:845–854
29. Reddy L, Endo T, Reddy GS (2012) Electronic (absorption) spectra of 3d transition metal complexes, chapter 1, advanced aspects of spectroscopy. Publisher: InTech